A long pathway of high water vapor from the Asian summer monsoon into the stratosphere

Paul Konopka, Christian Rolf, Marc von Hobe, Sergey Khaykin, Benjamin Clouser, Elizabeth Moyer, Fabrizio Ravegnani, Francesco d'Amato, Silvia Viciani, Nicole Spelten, et al.

HAL Id: insu-04072198

https://insu.hal.science/insu-04072198v1

Submitted on 17 Apr 2023 (v1), last revised 16 Oct 2023 (v2)

A long pathway of high water vapor from the Asian summer monsoon into the stratosphere

Paul Konopka[1], Christian Rolf[1], Marc von Hobe[1], Sergey M. Khaykin[3], Benjamin Clouser[4], Elizabeth Moyer[4], Fabrizio Ravegnani[5], Francesco D'Amato[6], Silvia Viciani[6], Nicole Spelten[1], Armin Afchine[1], Martina Krämer[1], Fred Stroh[1], and Felix Ploeger[1,2]

[1]Forschungszentrum Jülich, IEK-7, Jülich, Germany
[2]Institute for Atmospheric and Environmental Research, University of Wuppertal, Wuppertal, Germany
[3]Laboratoire Atmospheres, Observations Spatiales (LATMOS), CNRS/INSU, Sorbonne Universite, Guyancourt, France
[4]Department of the Geophysical Sciences, University of Chicago, Chicago, IL, USA
[5]National Research Council - Institute for Atmospheric Sciences and Climate (ISAC-CNR), 40129 Bologna, Italy
[6]National Institute of Optics, CNR-INO, Via Madonna del Piano 10, Sesto Fiorentino, Florence, Italy

Correspondence: Paul Konopka (p.konopka@fz-juelich.de)

Abstract. During the StratoClim Geophysica campaign, air with total water mixing ratios up to 200 ppmv and ozone up to 250 ppbv was observed within the Asian summer monsoon anticyclone up to 1.7 km above the local cold point tropopause (CPT). To investigate the temporal evolution of enhanced water vapor being transported into the stratosphere, we conduct forward trajectory simulations using both a microphysical and an idealized freeze-drying model. The models are initialized at the mea-

5 surement locations and the evolution of water vapor and ice is compared with satellite observations of MLS and CALIPSO. Our results show that these extremely high water vapor values observed above the CPT are very likely to undergo significant further freeze-drying due to experiencing extremely cold temperatures while circulating in the anticyclonic dehydrition carousel. We also use the Lagrangian dry point (LDP) of the merged backward and forward trajectories to reconstruct the water vapor fields. The results show that the extremely high water vapor mixed in with the stratospheric air has a negligible impact on the overall

10 water vapor budget. The LDPs are a better proxy for the large-scale water vapor distributions in the stratosphere during this period.

1 Introduction

Stratospheric water vapor (SWV) is a potent greenhouse gas with a significant radiative forcing (Forster and Shine, 1999; Solomon et al., 2010). In the tropical lower stratosphere, SWV values are determined primarily by the freeze drying of moist

15 tropospheric air entering the stratosphere at the cold point tropopause (CPT) (Randel and Park, 2019; Smith et al., 2021). The amount of ice injected into the stratosphere by deep, overshooting convection remains uncertain (Randel et al., 2012; Avery et al., 2017; Ueyama et al., 2020; Jensen et al., 2020). Recent in-situ measurements suggest convective moistening above the local tropopause in the Asian summer monsoon (ASM) region, while satellite observations show a drying effect of convection on a larger scale (Khaykin et al., 2022; Randel et al., 2015).

	Type A	Type B	Type M
Flights	10.08	29.07	08.08
Number of data	379	1834	102
Distance to CPT	0–0.25 km	0.0–1.7 km	1.1-1.3 km
75% of LDP ages	0 to 3 days	-35 to –15 days	bimodal
H_2O (gas)	3.4-6.1 ppm	7.0-10.2 ppm	6.9-7.3 ppm
H_2O (ice)	values up to 250 ppm	no ice observed	values up to 0.16 ppm
CO	32-93 ppb, strong spread	36-66 ppb, moderate variab.	23-40 ppb, weaker variab.
CO-ice correlation	positive and significant	no correlation	no correlation
HDO/H_2O, delta D	-700 to -300‰, strong spread	around -400‰, weaker variab.	around -480‰, moderate variab.

Table 1. Differences between type A and B of the moist and stratospheric air observed above the CPT. Type M shows mixed properties of type A ($\sim$30%) and B ($\sim$70%) with a bi-modal distribution of the LDP ages (Figure 1d) having maxima between -40 to -30 days ($\sim$75%) and around $\pm$1 day ($\sim$25%). Thus, while the LDPs of the type B air masses lie clearly in the past, type A may experience the strongest dehydration first in the future.

Lagrangian studies reconstruct SWV by tracking the minimum saturation mixing ratio of air at the Lagrangian dry point (LDP) (Fueglistaler and Haynes, 2005; Liu; Schoeberl and Dessler, 2011; Smith et al., 2021). We combine airborne in situ measurements during the StratoClim campaign in Nepal (Lauther et al., 2021) with satellite observations of MLS (Livesey et al., 2020) and CALIPSO (Vaughan et al., 2009) to investigate the representativeness of the moist air masses encountered above the CPT for the large-scale SWV distribution. Using forward trajectories and a microphysical model, we address two main questions: (i) How does the water vapor content of these air masses change during their ascent into the stratosphere? (ii) How representative are these air masses for the large-scale moisture budget of the lower stratosphere? Finally, we discuss the performance of LDP-based SWV reconstructions for these examples of moistening above the local CPT.

2 In situ data

During the StratoClim campaign, moist plumes with isotopic signatures of overshooting convection were detected above the local CPT in the ASM anticyclone (Khaykin et al., 2022). In this study, we use in situ data from Geophysica flights over Nepal and forward trajectories driven by the ERA5 reanalysis to assess the impact of these air masses on mean SWV values.

In Figure 1a, two thick black lines define data points that are "sufficiently moist" ($H_2O > 7$ ppm) and "sufficiently deep in the stratosphere" ($O_3 > 100$ ppb). Our data set is reduced to 2315 data points by only considering those observed above the CPT. We denote the data observed on 10.08 as type A and those observed on 29.07 as type B. The data observed on 08.08 (less than 5%) contain mixed properties of types A and B and are labeled as type M (see Table 1).
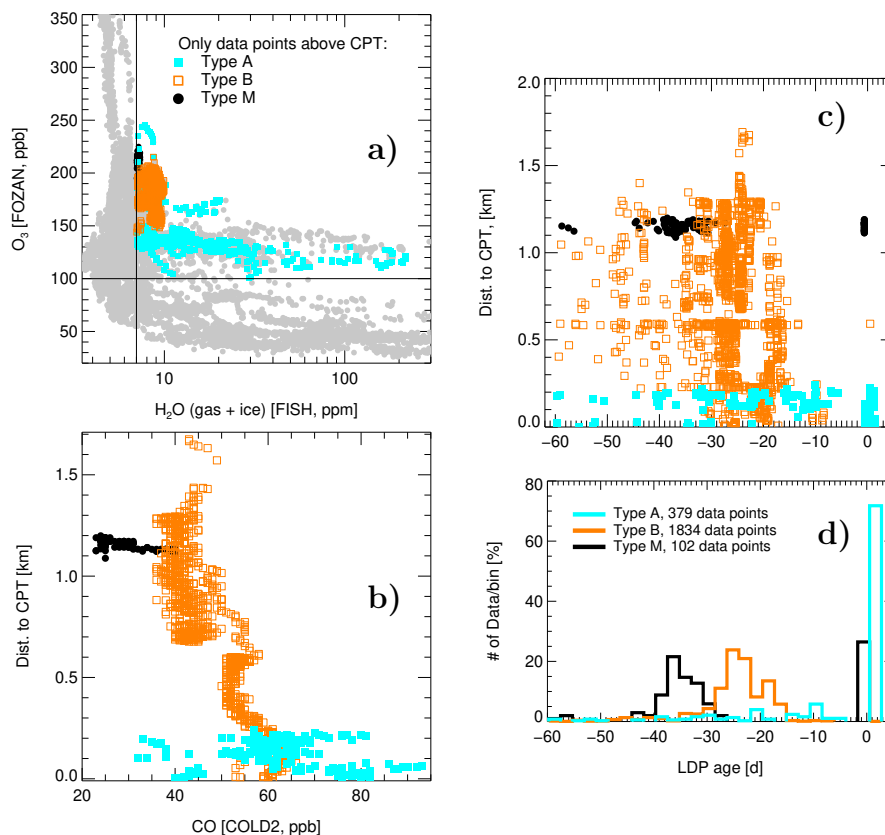
Figure 1. (a) H_2O-O_3 correlations for all local StratoClim flights (gray) with color-coded data points above the local cold point tropopause (CPT, derived from ERA5, see appendix) with mixing ratios of total $H_2O > 7$ ppm and with mixing ratios of $O_3 > 100$ ppm and divided into three groups: type A, type B, and type M. H_2O denotes the total water (gas + ice) observed by the Fast In situ Stratospheric Hygrometer (FISH), and O_3 denotes ozone sampled with the Fast-Response Chemiluminescent Airborne Ozone Analyzer (FOZAN). The FISH total water measurements inside of ice clouds are corrected for inlet ice particle enhancements after Afchine et al. (2018) by using the gas phase water the Fluorescent Lyman-Alpha Stratospheric Hygrometer (FLASH). For more details of FISH, FOZAN and FLASH instruments (Meyer et al., 2015; Khaykin et al., 2022). (b) For all three data types, distance to the CPT is shown as a function of CO sampled with the Carbon Oxide Laser Detector 2 (COLD2, Viciani et al. (2018)) and (c) as a function of the time distance to the Lagrangian dry point (LDP age), i.e. relative to the point with the minimum saturation mixing ratio over ice calculated along the merged back-and-forward ±60 days trajectories; negative/positive age means that LDP was found in the past/future. (d) The normalized frequency distributions of the LDP ages.

Figure 1b shows CO values for all three data sets as a function of distance to the CPT. CO decreases with altitude in slowly ascending air within the ASM anticyclone due to its chemical lifetime of a few months (von Hobe et al., 2021). This decrease can be seen for type B and M data, extending up to 1.7 km above the tropopause. Type A data are closer to the CPT and show fresh convection signatures, with a spread of CO values between 30 and 95 ppb, large spread of HDO/H_2O ratios, and positive

40 ice-CO correlations (see appendix). In Figure 1c, we compare the geometric distance of all data points relative to the CPT with the time distance to the LDP, quantified as LDP age. The LDP age does not necessarily decrease with the distance to the CPT, but instead shows a more complicated pattern. For type B data, LDP ages are between -15 and -35 days. For type A, more than 75% of the LDP encounters are still expected to occur along the forward trajectories, with LDP ages of 0-3 days, although these air parcels have been sampled above the local CPT.

45 ## 3 Dehydration scenarios along the forward trajectories

We use forward trajectories starting from the locations of the observed values of water vapor and ice for both types of air, A and B. Along these trajectories, we apply a state-of-the-art microphysical box model, CLaMS-Ice (see appendix), as well as a simple freeze drying model (FDM) that instantaneously removes excess water vapor along the forward trajectories when the air becomes supersaturated with respect to ice (FDM-forward). Figure 2a shows three exemplary forward trajectories: one of type
50 A and two of type B, that slowly ascend within the ASM anticyclone above the level of zero radiative heating (Vogel et al., 2019) with a rotation period of about 10 days (Legras and Bucci, 2020). All trajectories of type A and more than 85% of type B stay within the tropical band extending northward during the boreal summer up to ∼40N. Only ∼14% of the type B trajectories descend into the lowermost stratosphere (LMS) northward of ∼40N (see the second trajectory of type B) after being detached from the anticyclone. During their spiraling ascent, almost all trajectories repeatedly pass through regions with
55 low temperatures, well below 195 K, mainly on the south-east, south, and south-west flanks of the anticyclone, where water condensation and ice formation can occur. CLaMS-Ice and a simple freeze drying model (FDM) were used to simulate the trajectories and investigate dehydration scenarios. Figure 2d compares the models' results for one trajectory of type A with ice and water vapor observations from CALIPSO and MLS, respectively. CLaMS-Ice reproduces the CALIPSO ice observations fairly well, while FDM performs better in terms of water vapor comparison with MLS.

60 We extend the analysis to all type A and B forward trajectories initialized with in-situ observations of H_2O vapor and ice. Figure 3 displays the time-dependent frequency distribution at select times for type A (left) and type B (right). Relative to the initial distribution, the distributions derived from CLaMS-Ice and FDM evolve over time by moving to significantly lower values of total H_2O. Results of FDM are always drier than the results of CLaMS-Ice, where the interplay between condensation, evaporation, and sedimentation does not instantaneously remove ice from the air parcel like in FDM (see also Figure 2d). A
65 massive dehydration can be diagnosed for type A, affecting all air parcels, with mean/maximum values after 40 days of 5.0/11.3 ppmv (CLaMS-Ice) and 3.3/4.1 (FDM). The degree of dehydration for type B is weaker, as there are less than 1 ppm of ice at the initialization time. The mean/maximum values for type B after 40 days are: 8.1/9.8 ppmv (CLaMS-Ice) and 6.5/7.9 ppmv (FDM). Only 14% (CLaMS-Ice) and 1% (FDM) of the initial observations did not experience any dehydration. The final positions of these non-dehydrated air parcels are within the LMS.

70 The dehydration scenarios for type A and B are consistent with the respective frequency distributions of LDP temperatures from backward and forward trajectories (Figure 3). The strong dehydration of type A air masses, detrained very recently from fresh convection, is mainly due to the lowest temperatures (Lagrangian cold point) being experienced in the forward direction
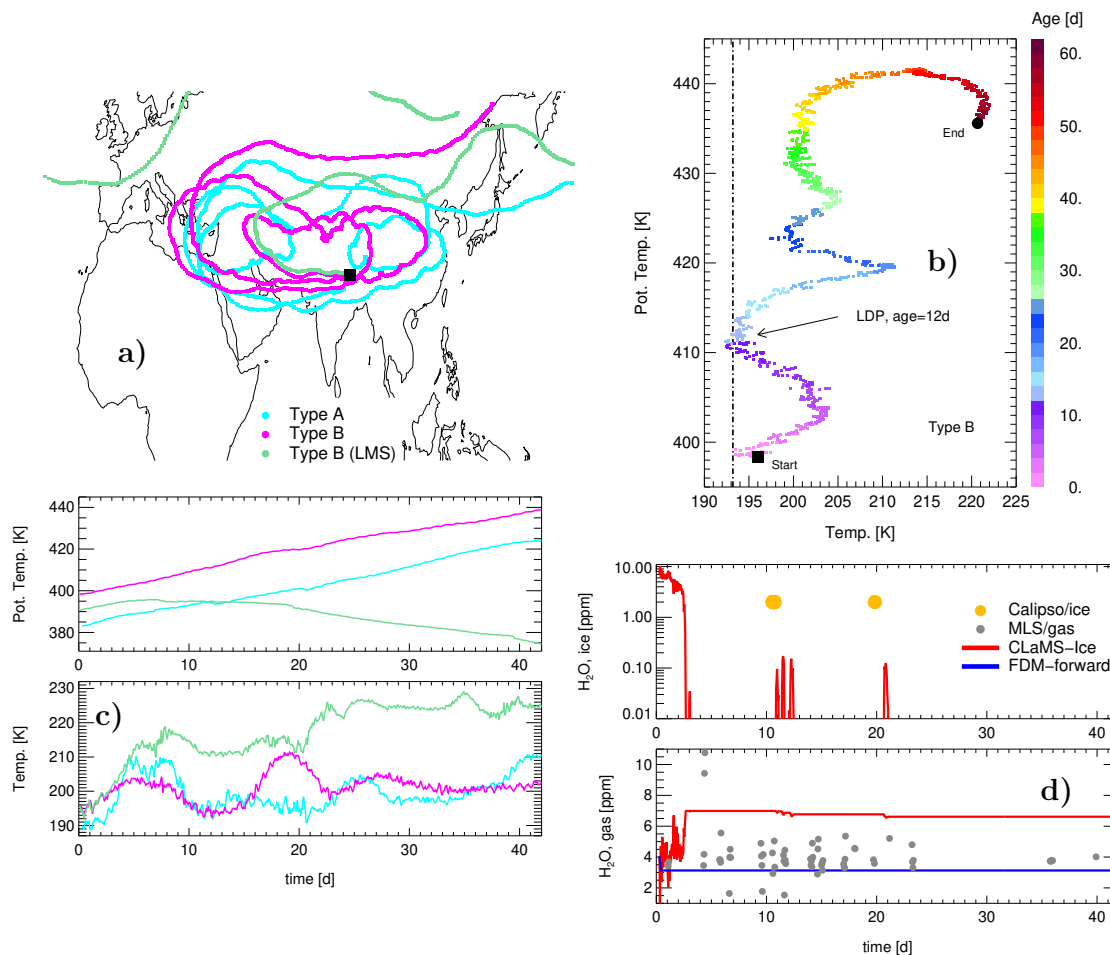
Figure 2. Box model studies of ice formation with CLaMS-Ice and with FDM-forward. Both models are initialized with data of type A and B as defined in Figure 1 (a) Three representative forward trajectories are shown: type A/B (cyan/pink) and one trajectory of type B that does not experience any dehydration and ends in the lowermost stratosphere (LMS, green). These three trajectories A, B and B (LMS) start form the observed values of H_2O (gas, in ppm: 7.13/9.06/10.0), H_2O (ice, in ppm: 4.05/0.03/0.00), O_3 (in ppb: 137/159/189) and CO (in ppb: 60,43,54) above the CPT (in km: 0.21/0.82/0.56). (b) Temperature evolution is color-coded with the LDP age for an upward spiraling trajectory of type B. (c) Time dependence of the potential temperature and temperature for all three trajectories. (d) Evolution of ice and gas phase along the type A trajectory as derived from CLaMS-Ice (red) and FDM (blue), both initialized from in-situ measurements, together with the CALIPSO observations of ice (yellow thick points, if CALIPSO found ice) and with the MLS observations of the gas phase in the vicinity of this trajectory (gray).

rather than in backward direction. On the other hand, most of the air masses of type B, detrained from convection several days to weeks before, have already experienced their lowest temperatures in the past (cf. Khaykin et al. (2022)). But even for type
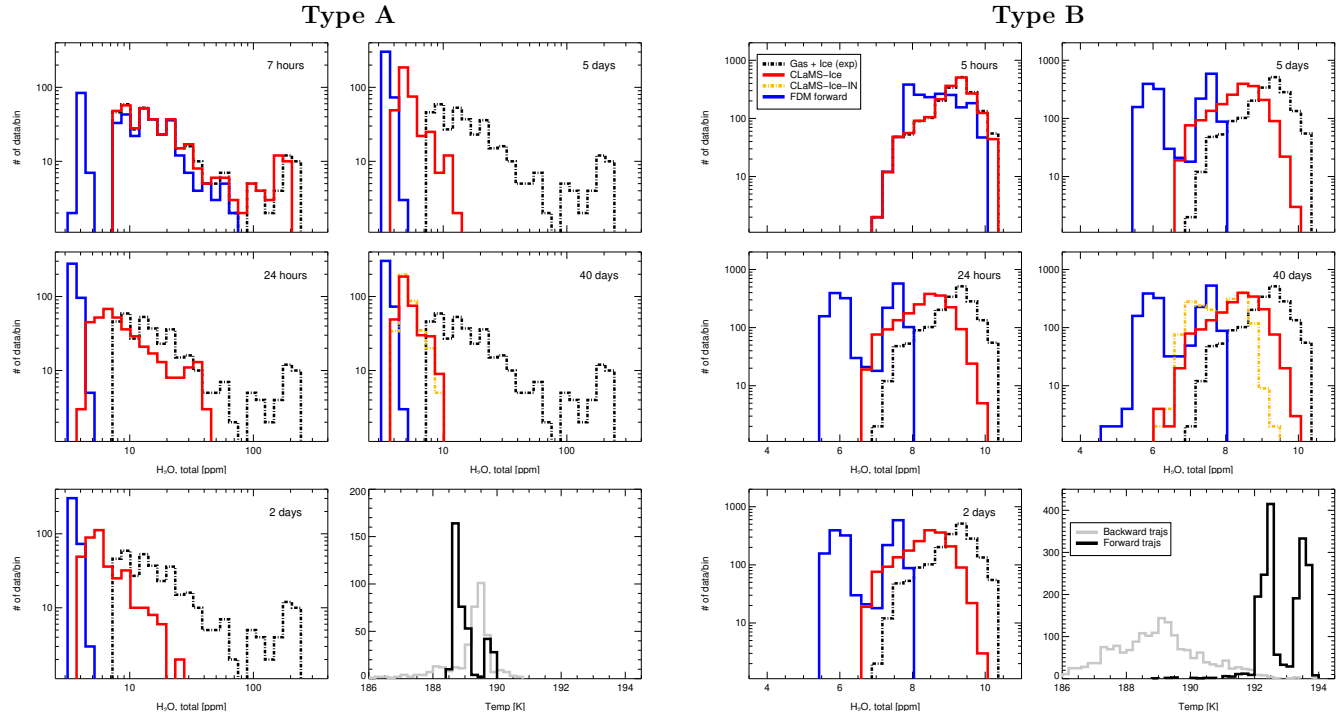
Figure 3. Time evolution of the total H_2O frequency distribution (number of data points per bin) starting from two in situ observed distributions (left/right, type A/B, dashed black) as derived from forward trajectory calculations using CLaMS-Ice (red), FDM-forward (blue), and from CLaMS-Ice with artificially enhanced heterogeneous ice nucleation (CLaMS-Ice-IN, orange); the latter is shown only 40 days after the initialization. For a better comparison, the initial frequency distribution is shown for all time steps (dashed black). Note that a logarithmic x-axis was applied for type A to take into account the large amount of ice used for initialization, while a simple linear x-axis was used for type B. The contribution of the dehydration driven by the parameterized gravity waves temperature fluctuations is very weak, as estimated from the small difference between the type B CLaMS-Ice distributions after 5 versus after 40 days (this difference vanishes if this parameterization is switched off). The 40-day distributions also show the impact of enhanced ice nucleation by using CLaMS-Ice-IN. The respective last panels show the frequency distribution of the LDP temperatures for the back and forward trajectories.

75 B air masses, a significant dehydration can still be expected in the future, well above the CPT, at the southern edge of the anticyclone during the upward spiraling motion of the forward trajectories, as seen from the shift of the frequency distributions to lower mixing ratios in the right panel of Figure 3.

4 Geographic perspective: Comparison with CALIPSO and MLS

We compare the ice distribution calculated by CLaMS-Ice during the dehydration periods along the forward trajectories with
80 CALIPSO observations, which detect ice mixing ratios larger than ~0.1 ppm (Avery et al., 2012). Figure 4 displays the results,
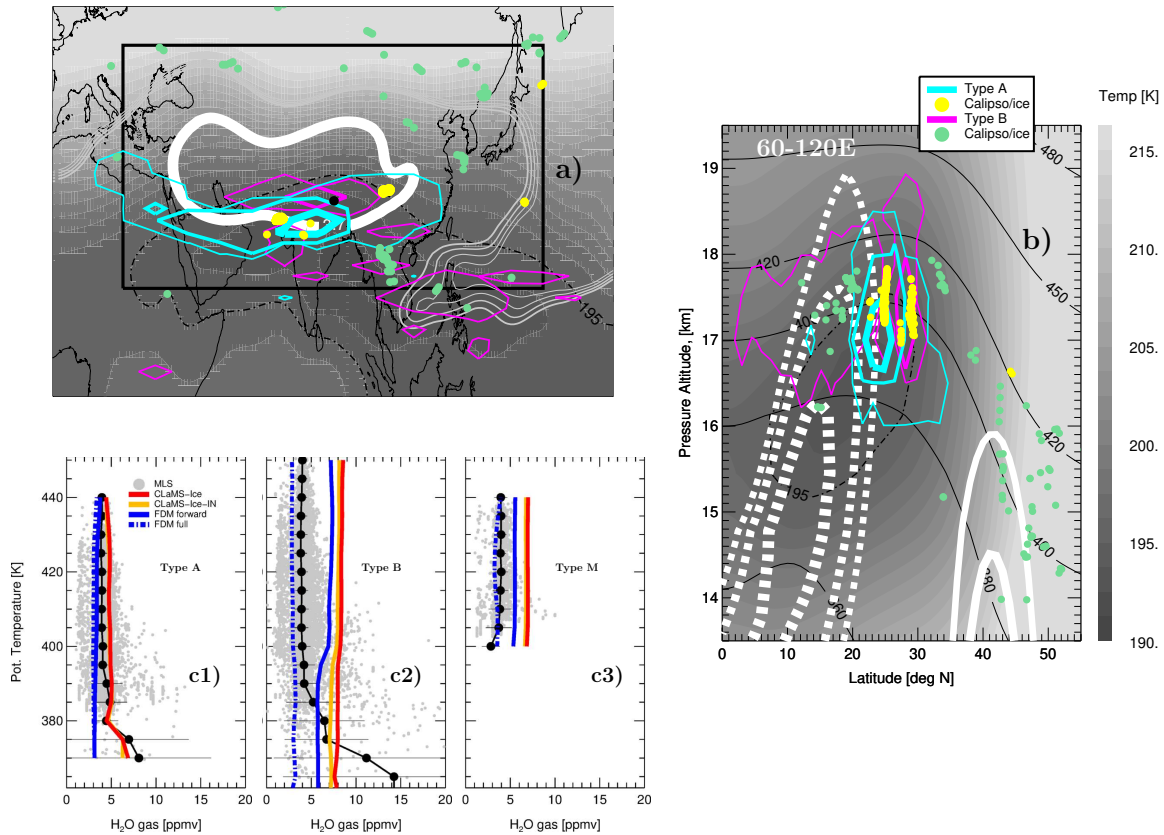
Figure 4. Geographic horizontal (a) and vertical (b) positions of ice formation (isolines of frequency distributions normalized by their total numbers) as derived from CLaMS-Ice applied along forward trajectories starting from the data sets A (cyan) and B (pink). The corresponding positions of CALIPSO ice observations in the vicinity of these trajectories are marked with yellow and green bold points. In the horizontal view (a), the edge of the ASM anticyclone (bold white) is derived from the gradient PV barrier at 380 K following the procedure described in Ploeger et al. (2017) (black filled circle - Kathmandu, the base of the StratoClim campaign). In the vertical view, the easterly and westerly jets (dashed and solid white lines) bound meridionaly the ASM anticyclone. As the ice clouds resolved by CLaMS-Ice are mainly driven by the experienced lowest temperatures, their geographic distribution is color-coded using a gray scale: (a) temperature minimum between potential temperature levels 360 and 420 K, (b) mean temperature averaged between 60-120 E, both from the ERA5 monthly mean for August 2017 with isolines for 195 K (dashed black). The other PV isolines at 380 K (light gray lines between 5.8 and 6.2 PVU in (a)) indicate the position of the dynamical tropopause. (c) Comparison with MLS for all trajectory parcels within the region confined by the black rectangle shown in (a) (gray – MLS data, black dots/horizontal lines – their mean values/standard deviations) split into data sets A, B, and M (c1-c3). Four models are used: CLaMS-Ice in the standard version (red), with the enhanced ice nuclei concentration (CLaMS-Ice-IN, orange) and by using a simply freeze drying model (FDM) along the forward and full trajectories (FDM forward/FDM full, solid/dashed blue).

where the horizontal (a) and vertical (b) large-scale temperature distributions are gray-coded and overlaid with the positions of the simulated and measured ice clouds, as well as the position of the ASM anticyclone (PV-based edge and the mean easterlies and westerlies) in August 2017. The comparison shows that type A generates significantly more ice than type B, and that type A agrees better with CALIPSO observations. Of the 442 type A ice events observed by CALIPSO, more than half are reproduced

85 by CLaMS-Ice, while of the 132 CALIPSO ice events of type B, less than 6% are simulated by CLaMS-Ice, despite data set B being ∼ 5 times larger. The geographic positions of type A ice clouds are also better reproduced, mainly found at 20N between 17 and 18 km altitude, with the strongest contribution over North India. In contrast, type B ice simulated by CLaMS-Ice shows a much larger horizontal spread, extending over the regions with coldest temperatures, mainly over southeast Asia and the Maritime Continent, and with weaker signatures. These signatures seem to be related to isentropic mixing driven by

90 Rossby waves, well-characterized by bent PV isolines surrounding the anticyclone (Konopka et al., 2009). There are a few weak CALIPSO signatures of ice in the LMS (type B) north of 35N between 400 and 420 K, which are not resolved by CLaMS-Ice. However, the expected warm temperatures in this part of the atmosphere raise some doubts about the origin of these signatures.

Complementary to ice, we also validate the calculated water vapor with the MLS observations along the forward trajectories.

95 While the comparison of CLaMS-Ice or FDM with MLS for the type A data is fairly good, there is a strong disagreement for the data of type B, even if ice nucleation in the model is enhanced (CLaMS-Ice-IN). A similarly strong disagreement between the model calculation and observations can be diagnosed if FDM-forward is used. Similar, but somewhat weaker disagreement was also found for the data of type M, consistent with fact that 30% and 70% of these data points are of type A and B, respectively. However, including dehydration also in the backward direction (FDM-full)), as used in many previous studies

100 (Fueglistaler and Haynes, 2005; Liu; Schoeberl and Dessler, 2011; Smith et al., 2021), performs extremely well for all three data types: A, B and M, especially in the region above 390 K (for sensitivity studies of this important result see appendix).

5 Discussion and conclusions

The mere existence of moist plumes over the CPT, which are also well above the lapse rate tropopause and therefore in the stratosphere, does not necessarily imply a persistent stratospheric moistening as significant dehydration events along the

105 forward trajectories are still possible. This is schematically shown in Figure 5, which contrasts the Eulerian view (with air masses being located above the CPT) and the Lagrangian view (with the LDP along the trajectory). Based on our case study using StratoClim data, the importance of considering the full Lagrangian air mass pathway in both backward and forward direction is clear not only for type A air masses, where the absolute LDPs are still ahead, but also for type B air masses, where the absolute LDPs have already occurred a few weeks prior. Even for these cases, multiple and subsequent dehydration

110 events at low temperatures, well below 195 K, can still be expected during the upward spiraling in the ASM anticyclone, with the highest ice concentration found mainly at its southern edge. Our simulations with CLaMS-Ice reproduce CALIPSO ice observations well for type A air masses, but the agreement for type B is worse (see Figure 4a and 4b). Note that the absolute LDPs of 75% of type A trajectories are in the future, with LDP ages ranging from 0-3 days. For type B trajectories, the LDPs
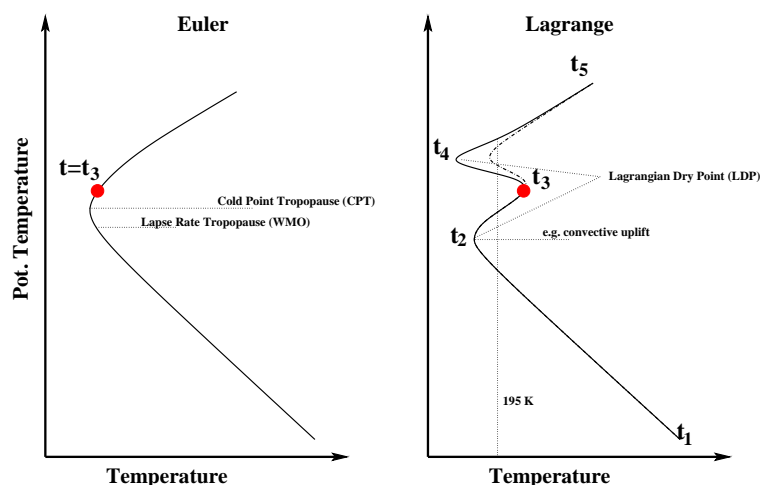
Figure 5. Lagrangian dry point (LDP) versus Eulerian cold point tropopause (CPT). Left: an idealized (Eulerian) temperature profile at time $t = t_3$ with an air parcel (shown in red) above the CPT (and above the lapse rate tropopause). Right: the corresponding (idealized) Lagrangian trajectory of this air parcel. A deep convective uplift between $t = t_1$ and $t = t_2$, with $t_2 - t_1$ being on the order of minutes to hours, may lift this air parcel into the stratosphere, i.e. above the local CPT. However, an additional temperature minimum can also be expected along the trajectory in the following time, i.e. at $t = t_4$, with $t_4 - t_2$ being on the order of days to weeks. This absolute (solid) or relative (dashed) minimum marks the respective absolute or relative LDP. Such additional LDPs were diagnosed for almost all air masses during their spiraling ascent within the ASM anticyclone. The freeze drying at these LDPs (if not happened before) defines the maximum amount of H_2O entering the stratosphere around $t = t_5$. Thus, pronounced ice formation events are expected at times t_2 and/or t_4, while pure water vapor can be assumed for $t = t_5$.

have already occurred in the past, with ages ranging from -35 to -15 days. It is worth noting that neither FDM applied to the
forward trajectories nor FDM applied to the full backward and forward trajectories can reproduce any CALIPSO ice signatures,
as ice is instantaneously formed and removed (i.e., not present) in this simple model setup.

However, if larger (synoptic) scales are considered, comparison with MLS is more relevant. MLS has a much coarser
sampling resolution compared to CALIPSO, which can resolve ice clouds extending over only a few tens of meters. While
the agreement between all our models and the mean MLS observations is sufficiently good for the type A data, for the air
masses of type B, all modeling approaches including only forward trajectories overestimate MLS by 3-4 ppm on average (see
Figure 5c). As all observations of type B occurred about 2-4 weeks after the absolute LDPs were passed (derived from the full
backward and forward trajectories), the in situ observed moist plumes are much wetter than the respective mixing ratios derived
from the LDPs along only forward trajectories. The dehydration events experienced along the forward trajectories, although
significant, are not able to freeze out the excess water vapor that is also not observed by MLS. This wet bias relative to the MLS
observations cannot be removed even if CLaMS-Ice-IN is applied, artificially enhancing dehydration to the highest realistic
limits. Only including dehydration along backward trajectories results in good agreement with MLS water vapor measurements.

In summary, small-scale moist plumes observed above the CPT are not necessarily representative of the large-scale distribution of SWV, in particular in the Asian monsoon region where the anticyclonic flow in the UTLS is regionally confined and close to low temperatures. In particular, moist plumes observed above the CPT, which likely result from convective overshoots, are not representative of the large-scale budget of SWV.

This important result requires some critical remarks. First, our study is only a case study showing that such events are possible. Second, there are other regions in the world, like e.g. the American monsoon, where ice transport into the stratosphere is more likely (Jensen et al., 2020; Park et al., 2021), and, consequently, such small-scale features may have stronger influence on the large-scale water vapor distribution. Here, additional case studies following our ideas could help. Despite these caveats, our results support some criticism related to the representativeness of the high-resolution, in situ data, like those of the longest available record of the balloon-borne NOAA frost point hygrometer over Boulder, for the quantification of the SWV trends (Kunz et al., 2013; Hegglin et al., 2014; Lossow et al., 2017; Konopka et al., 2022). Our study shows that moist plumes can be sampled in the stratosphere which are not representative for the large-scale distributions of SWV. The fact that stratospheric satellite instruments capable of measuring SWV concentrations are approaching the end of their life time emphasizes the importance of setting up in-situ observation networks (e.g. using stratospheric balloons) with regular and "statistically robust" sampling (Müller et al., 2016).

Finally, a few remarks are necessary regarding the performance of our most idealized modeling approach, reconstructing the SWV from the absolute LDP derived from full backward and forward trajectories covering several weeks. This method of SWV reconstruction works throughout the lower tropical stratosphere, taking into account only the time evolution of temperatures at the CPT, a 2D surface. That is, the trajectory-based reconstruction propagates a 2D minimum saturation mixing ratio into the full 3D space. As the quality of tropopause temperatures has improved over the last decades, particularly for ERA5 (Tegtmeier et al., 2020), the quality of the reconstructed SWV has also improved. Our results show that tropopause temperatures exert a dominant control over the tropical stratosphere in the ASM region (Randel et al., 2015; Randel and Park, 2019), and this dominance seems to be more representative of global SWV values than sporadic observations of moist plumes in the stratosphere. However, we also found that the SWV reconstruction is not as effective for trajectories ending in the LMS (see Appendix). In this region, the final values of SWV are not only controlled by LDPs, but also by other processes such as mixing or downward transport of SWV affected by methane oxidation.

Appendix A: In-situ data, trajectory and CLaMS-Ice calculation

Figure A1 completes the experimental data shown in Figure 1 by including the observed isotopic ratios of water (HDO/H_2O) and by showing the CO-ice correlations for data of type A in panels (a) and (b), respectively.

Both forward and backward 60-days trajectories used in this study start at the space-time coordinates of the in-situ observations collected on board of the Geophysica and are calculated with the trajectory module of the Chemical Lagrangian Model of the Stratosphere (CLaMS) (McKenna et al., 2002), driven by the ERA5 horizontal wind velocities (Hersbach et al., 2020) and the diabatic heating rates (Ploeger et al., 2010) with the highest available spatial (0.3×0.3 degree, 137 model levels) and tem-
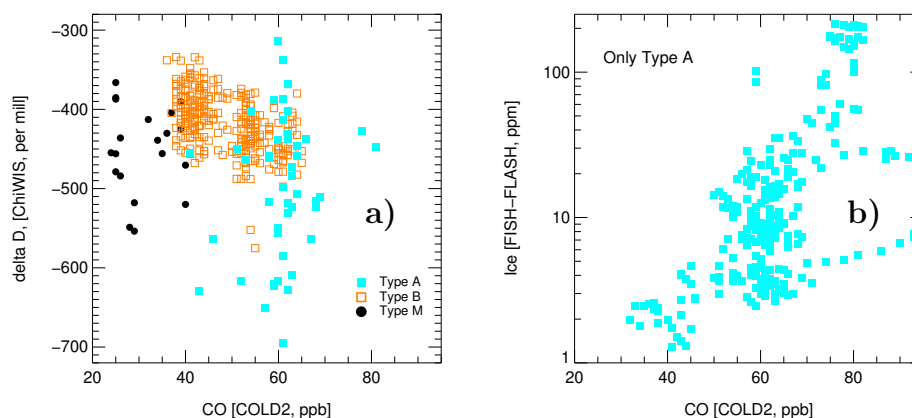
Figure A1. (a) CO-delta D correlation for data types A, B and M with the same notation as in Figure 1. Delta-D quantifies the observed isotopic ratios of water (HDO/H_2O) measured by the Chicago Water Isotope Spectrometer (ChiWIS). Delta-D values are enhanced (larger than -450‰) for water vapor molecules sublimated from ice with convective origin and which are depleted (smaller than -550‰) for data points characterizing the stratospheric background. Thus, water vapor of type B (and partially of type M) originated from convective ice clouds which have evaporated in the last 60-20 days. On the other hand, air masses of type A (and partially type M) show signatures of fresh convection, with a larger spread of delta-D values, indicating that the transition from the ice to the gas phase is only partially completed (Moyer et al., 1996; Sarkozy et al., 2020; Khaykin et al., 2022) (b). Positive CO-ice correlations for data of type A point also to fresh convection as a possible explanation.

160 poral (1 hour) resolution of the meteorological data (Hoffmann et al., 2019). The vertical distance to the CPT is defined as the geometric distance between the Geophysica flight track and the temperature minimum in the ERA5 temperature profiles interpolated to the Geophysica flight track while the LDP is found as the minimum saturation mixing ratio over ice, calculated from the ERA5 temperature and pressure (Sonntag, 1994), interpolated along the forward, backward, and merged back-and-forward trajectories starting at the flight track.

165 CLaMS-Ice takes into account all relevant microphysical processes important for hydration and dehydration of air, such as nucleation of ice, diffusional growth, sublimation, and sedimentation processes that change the amount of water vapor and ice in the air parcel moving along the trajectory. The model, based on the two-moment scheme published by Spichtinger and Gierens (2009), has been extensively validated against measurements in cloud chamber experiments (Baumgartner et al., 2022). Although the ERA5 temperature interpolated along the trajectory is the main driver of all these processes, it can also be overlaid

170 with temperature fluctuations induced by unresolved gravity waves in the coarser meteorological fields, following the method described in Podglajen et al. (2016). CLaMS-Ice is initialized at the beginning of the forward trajectories with the in-situ observations, i.e. ice water content derived from the combination of FISH and FLASH instruments and ice particle number concentration in the range of 3-937 μm form the New Ice eXpEriment-Cloud and Aerosol Particle Spectrometer (NIXE-CAPS) (Krämer et al., 2016).

Appendix B: Sensitivity studies

To find the "nearest" CALIPSO and MLS data points, both in time and space, three types of match criteria were applied: strong, moderate, and weak. All three match criteria are defined by different values of the distance in space and time between the trajectory position and the respective CALIPSO/MLS overpass with Δt=1h, 2h, 4h, r=30, 50, 150 km for CALIPSO and Δt=1h, 2h, 3h, r=100, 150, 200 km for MLS. The vertical match criteria are 60 m and 20 hPa for CALIPSO and MLS, respectively. The moderate version of the data match is used as the default, as it is a compromise between the number of matches and their quality. Figure B1 supports the results shown in Figure 4 by discussing the sensitivity of the presented results to the
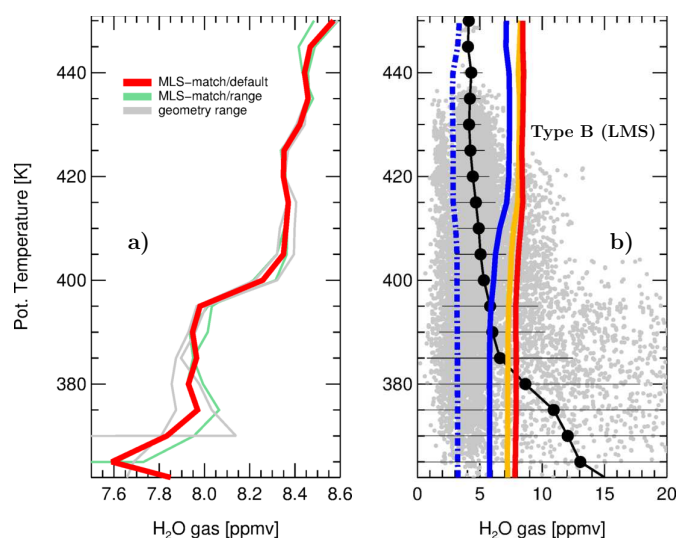

Figure B1. Sensitivity studies of dehydration scenarios and their validation with MLS. (a) Investigation of sensitivity to the match criterion (strong, moderate, and weak) and to the choice of the rectangle bounding the ASM anticyclone shown in Figure 4a. (b) Validation of four models for the subset of type B trajectories that end not in the rectangle bounding the ASM anticyclone, but in the LMS. Note that this represents less than 15% of type B trajectories. The figure shows that the FDM-full model disagrees with MLS observations between 380 and 420 K, which could be due to omitted processes such as mixing or downward transport of water vapor created by methane oxidation, or due to reduced MLS performance in this part of the atmosphere (for the legend, see Figure 4c1).

choice of few crucial parameters and by analyzing the model representation of air masses with forward trajectories ending in the LMS.

12

Code and data availability. The trajectrory module is a part of CLaMS-2.0/MESSy code based on MESSy version 2.54 and accessible for MESSy consortium members at https://gitlab.dkrz.de/MESSy. The usage of MESSy and access to the source code is licensed to all affiliates of institutions which are members of the MESSy Consortium. Institutions can become a member of the MESSy Consortium by signing the MESSy Memorandum of Understanding. More information can be found on the MESSy Consortium Website (http://www.messy-interface.org, last access: 30 June 2022). ERA5 model level reanalysis data are available from the ECMWF as deterministic forecasts (atmospheric model): via: https://apps.ecmwf.int/data-catalogues/era5/?class=ea. The StratoClim data can be downloaded from: http://www.stratoclim.org/. For more detailed model data, please contact the authors.

Competing interests. Marc von Hobe and Martina Krämer are members of the editorial board of Atmospheric Chemistry and Physics.

References

205

Afchine, A., Rolf, C., Costa, A., Spelten, N., Riese, M., Buchholz, B., Ebert, V., Heller, R., Kaufmann, S., Minikin, A., Voigt, C., Zöger, M., Smith, J., Lawson, P., Lykov, A., Khaykin, S., and Krämer, M.: Ice particle sampling from aircraft – influence of the probing position on the ice water content, Atmospheric Measurement Techniques, 11, 4015–4031, https://doi.org/10.5194/amt-11-4015-2018, 2018.

Avery, M., Winker, D., Heymsfield, A., Vaughan, M., Young, S., Hu, Y., and Trepte, C.: Cloud ice water content retrieved from the CALIOP
210   space-based lidar, Geophysical Research Letters, 39, https://doi.org/https://doi.org/10.1029/2011GL050545, 2012.

Avery, M., Davis, S., Rosenlof, K. H., Ye, H., and Dessler, A. E.: Large anomalies in lower stratospheric water vapour and ice during the 2015–2016 El Nino, Nature Geoscience, 10, 405 – 409, https://doi.org/10.1038/ngeo2961, 2017.

Baumgartner, M., Rolf, C., Grooß, J.-U., Schneider, J., Schorr, T., Möhler, O., Spichtinger, P., and Krämer, M.: New investigations on homogeneous ice nucleation: the effects of water activity and water saturation formulations, Atmospheric Chemistry and Physics, 22,
215   65–91, https://doi.org/10.5194/acp-22-65-2022, 2022.

Forster, P. and Shine, K. P.: Stratospheric water vapour change as possible contributor to observed stratospheric cooling, Geophys. Res. Lett., 26, 3309 – 3312, https://doi.org/10.1029/1999GL010487, 1999.

Fueglistaler, S. and Haynes, P. H.: Control of interannual and longer-term variability of stratospheric water vapor, Journal of Geophysical Research: Atmospheres, 110, https://doi.org/https://doi.org/10.1029/2005JD006019, 2005.

220 Hegglin, M. I., Plummer, D. A., Shepherd, T. G., Scinocca, J. F., Anderson, J., Froidevaux, L., Funke, B., Hurst, D., Rozanov, A., Urban, J., von Clarmann, T., A.Walker, K., Wang, H. J., Tegtmeier, S., and Weigel, K.: Vertical structure of stratospheric water vapour trends derived from merged satellite data, Nature Geoscience, 7, 768–776, https://doi.org/10.1038/NGEO2236, 2014.

Hersbach, H., Bell, B., Berrisford, P., Hirahara, S., Horányi, A., Muñoz-Sabater, J., Nicolas, J., Peubey, C., Radu, R., Schepers, D., Simmons, A., Soci, C., Abdalla, S., Abellan, X., Balsamo, G., Bechtold, P., Biavati, G., Bidlot, J., Bonavita, M., De Chiara, G., Dahlgren, P., Dee,
225   D., Diamantakis, M., Dragani, R., Flemming, J., Forbes, R., Fuentes, M., Geer, A., Haimberger, L., Healy, S., Hogan, R. J., Hólm, E., Janisková, M., Keeley, S., Laloyaux, P., Lopez, P., Lupu, C., Radnoti, G., de Rosnay, P., Rozum, I., Vamborg, F., Villaume, S., and Thépaut, J.-N.: The ERA5 global reanalysis, Q. J. R. Meteorol. Soc., 146, 1999–2049, https://doi.org/https://doi.org/10.1002/qj.3803, 2020.

Hoffmann, L., Günther, G., Li, D., Stein, O., Wu, X., Griessbach, S., Heng, Y., Konopka, P., Müller, R., Vogel, B., and Wright, J. S.: From ERA-Interim to ERA5: the considerable impact of ECMWF's next-generation reanalysis on Lagrangian transport simulations, Atmos.
230   Chem. Phys., 19, 3097–3124, https://doi.org/10.5194/acp-19-3097-2019, 2019.

Jensen, E. J., Pan, L. L., Honomichl, S., Diskin, G. S., Krämer, M., Spelten, N., Günther, G., Hurst, D. F., Fujiwara, M., Vömel, H., Selkirk, H. B., Suzuki, J., Schwartz, M. J., and Smith, J. B.: Assessment of Observational Evidence for Direct Convective Hydration of the Lower Stratosphere, Journal of Geophysical Research: Atmospheres, 125, https://doi.org/https://doi.org/10.1029/2020JD032793, 2020.

Khaykin, S. M., Moyer, E., Krämer, M., Clouser, B., Bucci, S., Legras, B., Lykov, A., Afchine, A., Cairo, F., Formanyuk, I.,
235   Mitev, V., Matthey, R., Rolf, C., Singer, C. E., Spelten, N., Volkov, V., Yushkov, V., and Stroh, F.: Persistence of moist plumes from overshooting convection in the Asian monsoon anticyclone, Atmospheric Chemistry and Physics, 22, 3169–3189, https://doi.org/10.5194/acp-22-3169-2022, 2022.

Konopka, P., Grooß, J.-U., Plöger, F., and Müller, R.: Annual cycle of horizontal in-mixing into the lower tropical stratosphere, Journal of Geophysical Research: Atmospheres, 114, https://doi.org/https://doi.org/10.1029/2009JD011955, 2009.

240 Konopka, P., Tao, M., Ploeger, F., Hurst, D. F., Santee, M. L., Wright, J. S., and Riese, M.: Stratospheric Moistening After 2000, Geophysical
Research Letters, 49, e2021GL097 609, https://doi.org/https://doi.org/10.1029/2021GL097609, 2022.

Krämer, M., Rolf, C., Luebke, A., Afchine, A., Spelten, N., Costa, A., Meyer, J., Zöger, M., Smith, J., Herman, R. L., Buchholz, B., Ebert,
V., Baumgardner, D., Borrmann, S., Klingebiel, M., and Avallone, L.: A microphysics guide to cirrus clouds – Part 1: Cirrus types,
Atmospheric Chemistry and Physics, 16, 3463–3483, https://doi.org/10.5194/acp-16-3463-2016, 2016.

245 Kunz, A., Müller, R., Homonnai, V., M., Janosi, I., Hurst, D., Rap, A., M. Forster, P., Rohrer, F., Spelten, N., and Riese, M.: Extending water
vapor trend observations over Boulder into the tropopause region: Trend uncertainties and resulting radiative forcing, J. Geophys. Res. A,
118, 11,269–11,284, https://doi.org/https://doi.org/10.1002/jgrd.50831, 2013.

Lauther, V., Vogel, B., Wintel, J., Rau, A., Hoor, P., Bense, V., Müller, R., and Volk, C. M.: In situ observations of CH_2Cl_2 and $CHCl_3$ show
efficient transport pathways for very short-lived species into the lower stratosphere via the Asian and North American summer monsoons,
250 Atmos. Chem. Phys., 2021, 1–42, https://doi.org/10.5194/acp-2021-837, 2021.

Legras, B. and Bucci, S.: Confinement of air in the Asian monsoon anticyclone and pathways of convective air to the stratosphere during the
summer season, Atmospheric Chemistry and Physics, 20, 11 045–11 064, https://doi.org/10.5194/acp-20-11045-2020, 2020.

Livesey, N. J., Read, W. G., Wagner, P. A., Froidevaux, L., Santee, M. L., Schwartz, M. J., Lambert, A., Millan Valle, L. F., Pumphrey,
H. C., Manney, G. L., Fuller, R. A., Jarnot, R. F., Knosp, B. W., and Lay, R. R.: Version 5.0x Level 2 and 3 data quality and description
255 document, Tech. Rep. JPL D-105336 Rev. A, Jet Propulsion Laboratory, California Institute of Technology Pasadena, California, 91109-
8099, http://mls.jpl.nasa.gov, 2020.

Lossow, S., Khosrawi, F., Nedoluha, G. E., Azam, F., Bramstedt, K., Burrows, Dinelli, B. M., Eriksson, P., Espy, P. J., García-Comas, M.,
Gille, J. C., Kiefer, M., Noël, S., Raspollini, P., Read, W. G., Rosenlof, K. H., Rozanov, A., Sioris, C. E., Stiller, G. P., Walker, K. A., and
Weigel, K.: The SPARC water vapour assessment II: comparison of annual, semi-annual and quasi-biennial variations in stratospheric and
260 lower mesospheric water vapour observed from satellites, Atmos. Meas. Tech., 10, 1111–1137, https://doi.org/10.5194/amt-10-1111-2017,
2017.

McKenna, D. S., Konopka, P., Grooß, J.-U., Günther, G., Müller, R., Spang, R., Offermann, D., and Orsolini, Y.: A new Chem-
ical Lagrangian Model of the Stratosphere (CLaMS): 1. Formulation of advection and mixing, J. Geophys. Res., 107, 4309,
https://doi.org/10.1029/2000JD000114, 2002.

265 Meyer, J., Rolf, C., Schiller, C., Rohs, S., Spelten, N., Afchine, A., Zöger, M., Sitnikov, N., Thornberry, T. D., Rollins, A. W., Bozóki,
Z., Tátrai, D., Ebert, V., Kühnreich, B., Mackrodt, P., Möhler, O., Saathoff, H., Rosenlof, K. H., and Krämer, M.: Two decades of
water vapor measurements with the FISH fluorescence hygrometer: a review, Atmospheric Chemistry and Physics, 15, 8521–8538,
https://doi.org/10.5194/acp-15-8521-2015, 2015.

Moyer, E. J., Irion, F. W., Yung, Y. L., and Gunson, M. R.: ATMOS stratospheric deuterated water and implications for troposphere-
270 stratosphere transport, Geophysical Research Letters, 23, 2385–2388, https://doi.org/https://doi.org/10.1029/96GL01489, 1996.

Müller, R., Kunz, A., Hurst, D. F., Rolf, C., Krämer, M., and Riese, M.: The need for accurate long-term measure-
ments of water vapor in the upper troposphere and lower stratosphere with global coverage, Earth's Future, 4, 25–32,
https://doi.org/https://doi.org/10.1002/2015EF000321, 2016.

Park, M., Randel, W. J., Damadeo, R. P., Flittner, D. E., Davis, S. M., Rosenlof, K. H., Livesey, N., Lambert, A., and Read, W.: Near-
275 Global Variability of Stratospheric Water Vapor Observed by SAGE III/ISS, Journal of Geophysical Research: Atmospheres, 126,
e2020JD034 274, https://doi.org/https://doi.org/10.1029/2020JD034274, e2020JD034274 2020JD034274, 2021.

Ploeger, F., Konopka, P., Günther, G., Grooß, J.-U., and Müller, R.: Impact of the vertical velocity scheme on modeling transport in the tropical tropopause layer, Journal of Geophysical Research: Atmospheres, 115, https://doi.org/https://doi.org/10.1029/2009JD012023, 2010.

280   Ploeger, F., Konopka, P., Walker, K., and Riese, M.: Quantifying pollution transport from the Asian monsoon anticyclone into the lower stratosphere, Atmospheric Chemistry and Physics, 17, 7055–7066, https://doi.org/10.5194/acp-17-7055-2017, 2017.

Podglajen, A., Hertzog, A., Plougonven, R., and Legras, B.: Lagrangian temperature and vertical velocity fluctuations due to gravity waves in the lower stratosphere, Geophysical Research Letters, 43, 3543–3553, https://doi.org/https://doi.org/10.1002/2016GL068148, 2016.

Randel, W. J. and Park, M.: Diagnosing Observed Stratospheric Water Vapor Relationships to the Cold Point Tropical Tropopause, J. Geo-
285   phys. Res. A, 124, 7018–7033, https://doi.org/https://doi.org/10.1029/2019JD030648, 2019.

Randel, W. J., Moyer, E., Park, M., Jensen, E., Bernath, P., Walker, K., and Boone, C.: Global variations of HDO and HDO/H2O ratios in the upper troposphere and lower stratosphere derived from ACE-FTS satellite measurements, Journal of Geophysical Research: Atmospheres, 117, https://doi.org/https://doi.org/10.1029/2011JD016632, 2012.

Randel, W. J., Zhang, K., and Fu, R.: What controls stratospheric water vapor in the NH summer monsoon regions?, Journal of Geophysical
290   Research: Atmospheres, 120, 7988–8001, https://doi.org/https://doi.org/10.1002/2015JD023622, 2015.

Sarkozy, L. C., Clouser, B. W., Lamb, K. D., Stutz, E. J., Saathoff, H., Möhler, O., Ebert, V., and Moyer, E. J.: The Chicago Water Isotope Spectrometer (ChiWIS-lab): A tunable diode laser spectrometer for chamber-based measurements of water vapor isotopic evolution during cirrus formation, Review of Scientific Instruments, 91, 045 120, https://doi.org/10.1063/1.5139244, 2020.

Schoeberl, M. R. and Dessler, A. E.: Dehydration of the stratosphere, Atmospheric Chemistry and Physics, 11, 8433–8446,
295   https://doi.org/10.5194/acp-11-8433-2011, 2011.

Smith, J. W., Haynes, P. H., Maycock, A. C., Butchart, N., and Bushell, A. C.: Sensitivity of stratospheric water vapour to variability in trop-
ical tropopause temperatures and large-scale transport, Atmos. Chem. Phys., 21, 2469–2489, https://doi.org/10.5194/acp-21-2469-2021, 2021.

Solomon, S., Rosenlof, K., Portmann, R., Daniel, J., Davis, S., Sanford, T., and Plattner, G.-K.: Contributions of stratospheric water vapor to
300   decadal changes in the rate of global warming, Science, 327, 1219–1223, https://doi.org/10.1126/science.1182488, 2010.

Sonntag, D.: Advancements in the field of hygrometry, Meteorologische Zeitschrift, 3, 51–66, https://doi.org/10.1127/metz/3/1994/51, 1994.

Spichtinger, P. and Gierens, K. M.: Modelling of cirrus clouds – Part 1a: Model description and validation, Atmospheric Chemistry and Physics, 9, 685–706, https://doi.org/10.5194/acp-9-685-2009, 2009.

Tegtmeier, S., Anstey, J., Davis, S., Dragani, R., Harada, Y., Ivanciu, I., Pilch Kedzierski, R., Krüger, K., Legras, B., Long, C., Wang, J. S.,
305   Wargan, K., and Wright, J. S.: Temperature and tropopause characteristics from reanalyses data in the tropical tropopause layer, Atmos. Chem. Phys., 20, 753–770, https://doi.org/10.5194/acp-20-753-2020, 2020.

Ueyama, R., Jensen, E. J., Pfister, L., Krämer, M., Afchine, A., and Schoeberl, M.: Impact of Convectively Detrained Ice Crystals on the Humidity of the Tropical Tropopause Layer in Boreal Winter, Journal of Geophysical Research: Atmospheres, 125, e2020JD032 894, https://doi.org/https://doi.org/10.1029/2020JD032894, 2020.

310   Vaughan, M., Powell, K., Winker, D., Hostetler, C., Kuehn, R. E., Hunt, W., Getzewich, J., Young, S., Liu, Z., and McGill, M.: Fully automated detection of cloud and aerosol layers in the CALIPSO lidar measurements, J. Atmos. Ocean. Technol., 26, 2034–2050, https://doi.org/10.1175/2009JTECHA1228.1, 2009.

Viciani, S., Montori, A., Chiarugi, A., and D'Amato, F.: A Portable Quantum Cascade Laser Spectrometer for Atmospheric Measurements of Carbon Monoxide, Sensors, 18, https://doi.org/10.3390/s18072380, 2018.

315 Vogel, B., Müller, R., Günther, G., Spang, R., Hanumanthu, S., Li, D., Riese, M., and Stiller, G. P.: Lagrangian simulations of the transport of young air masses to the top of the Asian monsoon anticyclone and into the tropical pipe, Atmospheric Chemistry and Physics, 19, 6007–6034, https://doi.org/10.5194/acp-19-6007-2019, 2019.

von Hobe, M., Ploeger, F., Konopka, P., Kloss, C., Ulanowski, A., Yushkov, V., Ravegnani, F., Volk, C. M., Pan, L. L., Honomichl, S. B., Tilmes, S., Kinnison, D. E., Garcia, R. R., and Wright, J. S.: Upward transport into and within the Asian monsoon anticyclone as inferred

320 from StratoClim trace gas observations, Atmospheric Chemistry and Physics, 21, 1267–1285, https://doi.org/10.5194/acp-21-1267-2021, 2021.